Pathways for Oxygen Incorporation in Mixed Conducting Perovskites: A DFT-Based Mechanistic Analysis for (La, Sr)$MnO_{3-\delta}$

Yuri A. Mastrikov,[†,‡] Rotraut Merkle,[*,†] Eugene Heifets,[§] Eugene A. Kotomin,[†,§] and Joachim Maier[†]

Max-Planck-Institute for Solid State Research, Heisenbergstrasse 1, D-70569 Stuttgart, Germany, Institute for Solid State Physics, University of Latvia, Kengaraga Street 8, LV-1063 Riga, Latvia, and Materials Science and Engineering Department, University of Maryland, College Park, Maryland 20742-2115

Received: September 30, 2009; Revised Manuscript Received: December 11, 2009

An extensive set of DFT calculations on $LaMnO_3$ slabs has been generated and used as a basis to identify the most probable reaction mechanism for oxygen incorporation into (La, Sr)$MnO_{3-\delta}$ cathode materials. MnO_2[001] is found to be the most stable surface termination under fuel cell operation conditions (high temperature, high pO_2, cubic unit cell). Chemisorption leading to the formation of O_2^-, O_2^{2-}, and O^- atop Mn is exothermic, but due to the negative adsorption entropy and electrostatic repulsion the levels of coverage of molecular oxygen adsorbates are low (in the few percent range). Under typical solid oxide fuel cell conditions, a mechanism in which the encounter of O^- with a surface oxygen vacancy at the surface is rate-determining exhibits the fastest rate. The variation of the reaction rate and preferred mechanism(s) with adsorbate and point defect concentrations is discussed.

1. Introduction

The motivation for investigating the oxygen incorporation reaction into oxides is twofold. On one hand, it is of fundamental interest to understand the mechanism of one of the "simplest" chemical reactions in detail, including its dependence on the oxide's bulk and surface properties.[1] On the other hand, this process is of key importance for a variety of applications: directly, for the functioning of a number of electrochemical devices such as sensors and solid oxide fuel cell (SOFC) cathodes, but also indirectly, namely, for tailoring materials properties, aging, or degradation of functional ceramics.

As it is hardly possible to systematically analyze the mechanisms of device materials under operating conditions, one may instead study them under model conditions (an example is the analysis of the performance of (La, Sr)$MnO_{3-\delta}$ and (La, Sr)(Fe, Co)$O_{3-\delta}$ electrodes with well-defined geometry and morphology[2−7]) or even consider model materials such as Fe-doped $SrTiO_3$.[1−8] Unfortunately, the approach of "macroscopic kinetics" is often not able to resolve details on the microscopic level, such as the exact nature of intermediate species or transition states. The application of surface sensitive techniques for their identification or even quantification is limited by the requirement to work under conditions at least close to operating conditions, i.e., at elevated temperatures (typically 673−1073 K) and—most importantly—realistic oxygen partial pressures that are at least in the millibar range instead of UHV conditions. Thus, DFT calculations are an important tool for the detailed understanding of the oxygen incorporation reaction. This even holds true for the modeling of ideal perovskite surfaces that are expected to deviate from the actual systems under operating conditions. One has to keep in mind that the cation composition (and possibly even the crystallographic structure) of the first layer(s) of the oxide under SOFC operating conditions may differ from the bulk. This is expected to modify reaction barriers and point defect concentrations, but the reaction mechanism will still be a combination of the individual steps such as chemisorption, dissociation, surface diffusion, etc., as discussed here. Thus, the DFT results for the ideal perovskite surface are still relevant to a microscopic understanding of the oxygen incorporation reaction.

In this study, we investigate the oxygen surface reaction on pure and Sr-doped $LaMnO_3$, the first mixed conducting perovskite widely applied as a SOFC cathode material. The fact that the ionic conductivity of these manganites is low[9,10] does not necessarily imply that the reaction at the three-phase boundary or the bulk transport is limiting. Under certain conditions, the cathode process can also become limited by the oxygen incorporation surface reaction.[10,11] Recently we published DFT calculations of oxygen adsorption and defect migration on the $LaMnO_3$[001] surface.[12,13] Transition state calculations on the [110] and [100] surfaces of $LaMnO_3$ and $La_{0.5}Sr_{0.5}MnO_{3-\delta}$ have been carried out also by another group, but with thinner slabs and considerably smaller surface supercells and without detailed kinetic consideration of coupled elementary reaction and transport steps.[14−16] The fact that oxygen incorporation in refs 14 and 15 was studied on the highly polar and oxygen-deficient (La, Sr)MnO_3[110] termination has led to a much too exothermic reaction enthalpy and may be the reason for unexpected low (or even missing) reaction barriers.

In this paper, we performed additional calculations focusing on the key elements in the oxygen surface reduction, in particular, O_2 molecule surface diffusion and dissociation. Based on these data, we present and discuss for the first time a detailed *kinetic analysis* of different oxygen incorporation reaction pathways estimating the individual reaction rate of each step. We emphasize the importance of adsorbate coverage, surface oxygen vacancy concentration, and surface diffusion processes. We are aware that the surface composition and the structure of a real electrode may differ from the idealized treatment here.

* To whom correspondence should be addressed. E-mail: r.merkle@fkf.mpg.de. Tel.: +49 711 689 1768. Fax: +49 711 689 1721.
† Max-Planck-Institute for Solid State Research.
‡ University of Maryland.
§ University of Latvia.

10.1021/jp909401g
Published on Web 01/29/2010

Also, various DFT methodologies may yield different absolute energies, but on the other hand the energy differences are expected to be much more reliable. Thus, notwithstanding some uncertainties, we are convinced that the combination of DFT calculations and kinetic considerations gives valuable insight into the oxygen incorporation reaction mechanism (e.g., the importance of surface transport steps) and are indispensable complements to the experimental studies.

2. Computational Details

Similar to our previous studies, we employed the ab initio DFT computer code VASP 4.6.19 (ref 17) with a plane wave basis set (PAW method[18]) and with the GGA−Perdew−Wang-91 exchange-correlation potential[19] employing a cutoff energy of 400 eV and a 2 × 2 × 2 Monkhorst−Pack k-point mesh in the Brillouin zone.[20] Spin-polarized calculations of the $LaMnO_3$ bulk and the [001], [110] surfaces are in good agreement with experiment (when available).[21] In particular, for the low-temperature orthorhombic structure the A-type antiferromagnetic (AAF) configuration is the energetically most favorable, in agreement with experiment. The lattice constant of both the cubic (stable above 750 K) and orthorhombic phase exceeds the experimental value by only 0.5%. The calculated cohesive energy of 30.7 eV is close to the experimental value (31 eV). The calculated surface relaxation and surface energies shows a weak dependence on the magnetic configuration.[21,22] For slabs the ferromagnetic configuration has the lowest energy; thus, we performed all further calculations with collinear spins. One has also to keep in mind that relevant magnetic effects (≈0.1eV) are much smaller than the adsorption and migration energies under study (one to several electronvolts). However, complete neglect of spin polarization results in considerable errors in material properties. We studied both orthorhombic and cubic phases for the oxygen adsorption and thermodynamic stability of surfaces with adsorbates (sections 3.1, 3.2) but focused on the orthorhombic phase in the analysis of intermediates and transition states for the kinetic treatment (calculations for the defects/adsorbates in the high-temperature cubic phase[12] give qualitatively similar results; in particular, the O adsorption energy atop Mn increases by ≈3% only).

We found that seven- and eight-plane slabs are thick enough to show convergence of the main properties. The periodically repeated slabs were separated by a vacuum gap of 15.8 Å. All atomic coordinates in a slab were allowed to relax. The eight-layer slab $(LaOMnO_2)_4$ has the proper cation ratio and oxygen stoichiometry (all Mn atoms are in the formal +3 oxidation state) but exhibits a nonzero slab dipole moment and is terminated by different planes (MnO_2 and LaO). This is avoided in the symmetric seven-layer slab $MnO_2(LaOMnO_2)_3$, but it has a Mn excess relative to La and a higher oxygen content. This slightly affects the energy for dissociative oxygen adsorption on the MnO_2[001] surface

$$O_2 + 2Mn^{x}_{Mn} \rightleftharpoons 2O^{-}_{ad} + 2Mn^{\cdot}_{Mn} \quad (1)$$

which is −2.7 eV for the $(LaOMnO_2)_4$ slab and −2.2 eV for the symmetrical $MnO_2(LaOMnO_2)_3$ slab.[12] Both because of reduced computation time for the symmetrical configuration and because a symmetrical slab allows decoupling effects of different surface terminations, all further calculations refer to the seven-layer slabs.

The choice of the $2\sqrt{2} \times 2\sqrt{2}$ surface supercell for the calculation of adsorbates/surface defects corresponds to a coverage of 12.5%. Several test calculations were performed for a smaller coverage of 5%. All concentrations (designated by square brackets) are given as particle numbers per surface or bulk unit cell comprising one $LaMnO_3$ formula unit. The reaction barriers were calculated using the nudged elastic band method.[23] The effective charges on ions were calculated according to the Bader (topological) analysis.[24] Note that the effective charges both in the bulk and on the surfaces of $LaMnO_3$ are far from the formal charges, viz., +2.13 e_0 for La, +1.85 e_0 for Mn, and −1.29 e_0 for O.[12,21,22] The considerable contribution of the covalence effects in Mn−O chemical bonding makes classical force-field calculations of these systems and especially of diffusion-controlled processes therein a nontrivial task.

3. Results and Discussion

3.1. Stability of Surface Terminations. Oxygen incorporation into crystals begins at surfaces. Therefore, we commence with determining which $LaMnO_3$ surfaces are the most stable ones at a given temperature and oxygen partial pressure. Besides finding the structure with the lowest internal energy, this includes stability with respect to exchange with atoms between the bulk of the crystal, its surface, and the gas phase. This requires the calculation of the surface Gibbs free energy Ω^i of the various surface terminations. Details of the Ω^i calculations are summarized in ref 21 and the Supporting Information. The most important approximation in this treatment is that not only the differences in the vibrational contributions but also absolute vibrational contributions (due to removal of atoms) were neglected to be able to compare slabs with different stoichiometries. This seemingly drastic approximation can be justified by an estimate of these quantities which are typically found to be 10 meV/Å^2 [25,26] corresponding to 0.16 eV per surface unit cell (16 Å^2). Exact calculations of the vibrational contribution for defective perovskite surfaces lie well beyond current computational possibilities. First attempts are performed so far only for defect-free bulk perovskites.[27] While this estimated contribution is not completely negligible (it is to be regarded as an "error bar" on the stability lines in Figures 1 and 2), it does not exceed the typical DFT errors. The latter depend very much on the particular material. We estimated the average DFT error in calculations of formation enthalpies for a series of oxides relevant for $LaMnO_3$ as 0.7 eV[12] and took account of it, e.g., in Figure 3. In the regions where certain surfaces are the most stable, their Ω^i values are the lowest. These regions are painted in various colors in Figure 1. The variation of oxygen atom chemical potential $\Delta\mu_O$ with temperature and oxygen pressure pO_2 can be taken from experimental data[28] (for details, see ref 21 and the Supporting Information).

Figure 1 shows the stability diagram of different $LaMnO_3$ surface terminations for the low-temperature orthorhombic and high-temperature cubic phases. For a better understanding, we added also their cross sections (Figure 2) at $T = 1200$ K and oxygen partial pressure $pO_2 = 0.2$ bar, i.e., in the range of typical SOFC operating conditions. The surface stability regions in the diagrams are limited by lines 2, 6, and 4 which correspond to lines where coexistence with La_2O_3, MnO_2, and Mn_3O_4, respectively, occurs. Correspondingly, at the cross sections of the diagrams (Figure 2), the stability region lies between lines 2 and 6. Because of the DFT deficiencies in describing the relative energies for materials with different degrees of oxidation, we should treat the obtained data with some precaution. Thus, we highlighted lines where three-valent metal oxides La_2O_3 and Mn_2O_3 (solid lines 2 and 5) begin to precipitate out of the perovskite. In these oxides, metal oxidation numbers coincide with the oxidation states for these metals in $LaMnO_3$.

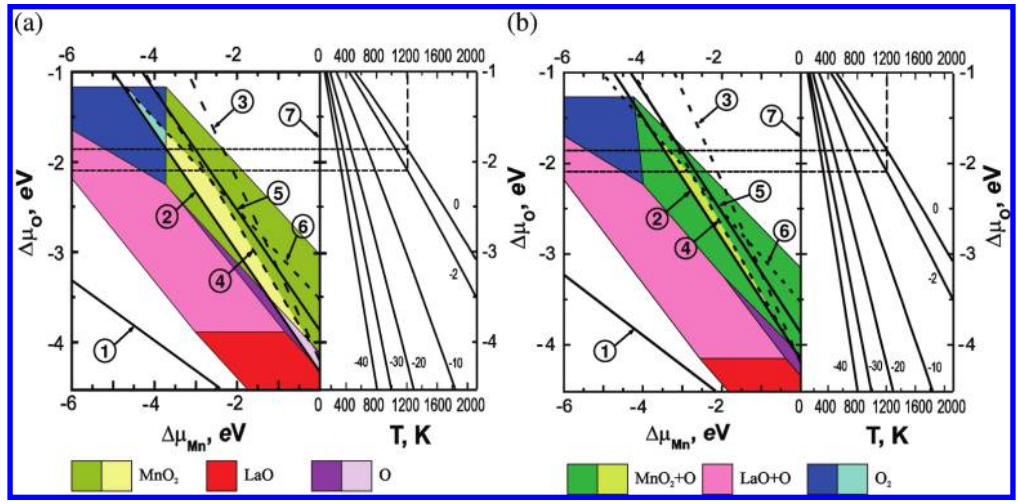

Figure 1. Phase diagrams: the regions of stability of $LaMnO_3$ surfaces with different terminations (LaO- and MnO_2-terminated [001] surfaces without and with adsorbed O atom, O_2- and O-terminated [011] surfaces) for both phases as functions of chemical potential variations for manganese and oxygen atoms. Parameters for all lines on the left side of the figures are collected in ref 21 and Table A1 of the Supporting Information. The numbers in circles point to lines where metals or their oxides begin to precipitate: (1) metal La, (2) La_2O_3, (3) MnO, (4) Mn_3O_4, (5) Mn_2O_3, (6) MnO_2, and (7) metal Mn. The right side of the figures contains a family of $\Delta\mu_O$ as functions of temperature at various oxygen gas pressures according to eq A.15 of the Supporting Information. The labels m on the lines represent the pressure: $pO_2 = 10^m$ bar. (a) Orthorhombic phase. (b) Cubic phase.

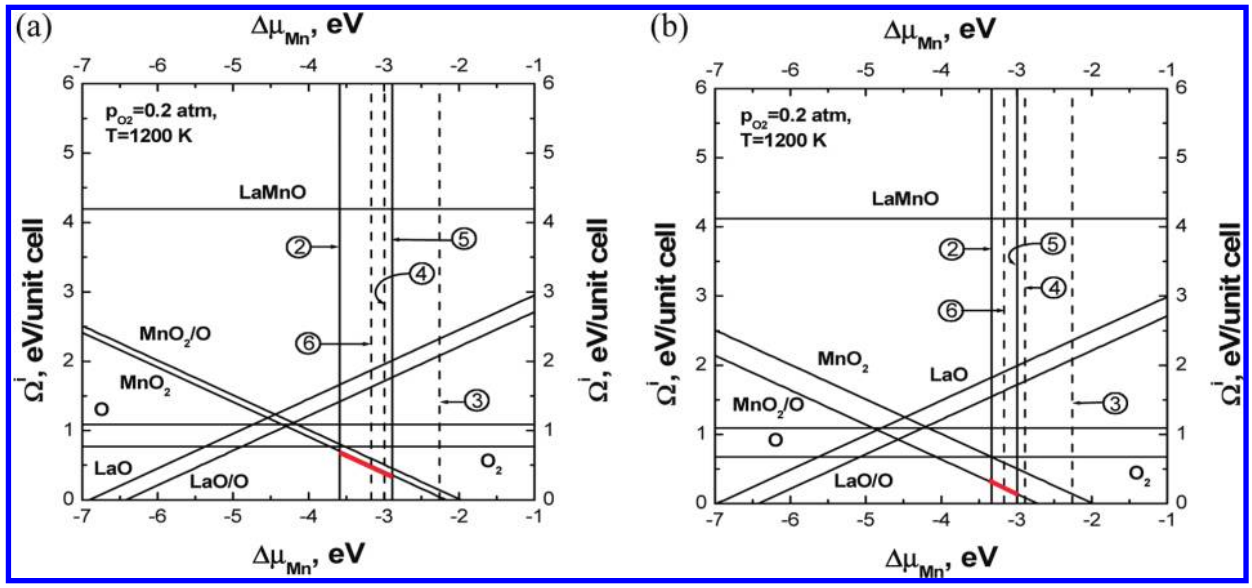

Figure 2. Surface Gibbs free energies Ω^i for $LaMnO_3$ in (a) orthorhombic and (b) cubic phases as functions of $\Delta\mu_{Mn}$ at $T = 1200$ K and $pO_2 = 0.2$ bar. Line numbers are the same as in Figure 1. The red lines indicate the most stable surface in the stability window between the precipitation lines for La_2O_3 and Mn_2O_3.

The most important conclusion from Figures 1 and 2 is that, for both phases, the most stable surface is MnO_2-terminated [001]. For the orthorhombic phase (on which we focus in the further analysis of reaction steps and rates), the stable surface is the clean MnO_2-terminated surface, whereas for the high-temperature cubic phase the most stable surface carries adsorbed O atoms. This indicates that for identical conditions higher adsorbate coverage is expected for the cubic phase.

3.2. Reaction Energies: Thermodynamic Picture. Let us consider formation of relevant oxygen species and point defects in the bulk and at the $LaMnO_3$ surface. We use the same approximation as in the previous subsection; that is, we neglect the changes of vibrational entropy in the solid, and thus only states comprising gaseous O_2 exhibit a temperature-dependent Gibbs free energy contribution. In this approximation, differences between Gibbs energies for bulk crystals or slabs (including defects and adsorbates) could be replaced with the differences in the total energy calculated from the DFT, while variation of oxygen chemical potential for gaseous O_2 is taken from experimental data. The Gibbs free energy of reaction for removal of 1/2 O_2 from the bulk (i.e., formation of one $V_O^{\cdot\cdot}$ and allocation of the left-behind two electrons mainly on Mn) is defined as

$$\Delta_f G_{bulk}(V_O^{\cdot\cdot}) = E_{bulk}(V_O^{\cdot\cdot}) + \mu_O(T, pO_2) - E_{bulk} \qquad (2)$$

where $E_{bulk}(V_O^{\cdot\cdot})$ is the total energy per bulk supercell with an oxygen vacancy, E_{bulk} is the total energy of the same supercell for the perfect crystal, and μ_O is the chemical potential of oxygen in the gas phase (O atoms in O_2 molecules). This definition can be rewritten as

$$\Delta_f G_{bulk}(V_O^{\cdot\cdot}) = \Delta_f E^{DFT}_{bulk}(V_O^{\cdot\cdot}) + \Delta\mu_O(T, pO_2) \qquad (3)$$

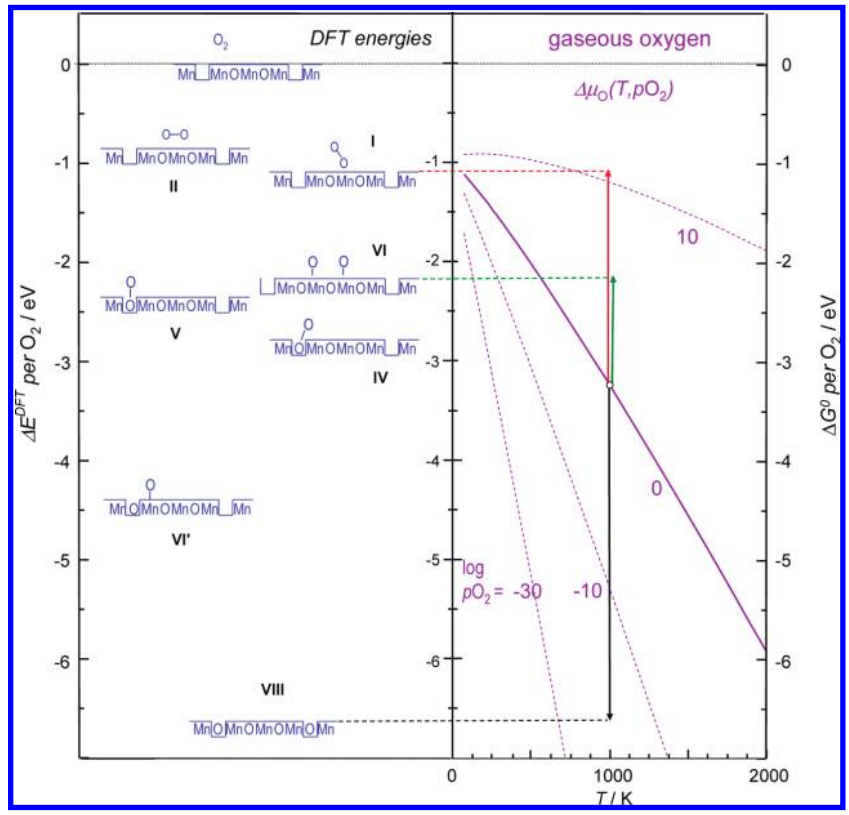

Figure 3. Left panel: DFT energy levels of different molecular and atomic species occurring during oxygen incorporation reaction on the MnO_2[001]-terminated surface of $LaMnO_3$, cf. Table 1. All energies are relative to the reference state containing two oxygen vacancies and a gas-phase O_2 molecule. The right panel shows the T and pO_2 dependence $\Delta\mu_O(T, pO_2)$ of the Gibbs energy of gaseous O_2 (see eq 3); its energy scale refers to an O_2 molecule. Labels m on the lines indicate oxygen pressure $pO_2 = 10^m$ bar. The arrows indicate various Gibbs free reaction energies at typical SOFC operating conditions: red = formation of adsorbed superoxide O_2^- without involvement of $V_O^{\cdot\cdot}$; green = formation of two adsorbed O^- atop Mn without involvement of $V_O^{\cdot\cdot}$; black = incorporation of O_2 into two surface oxygen vacancies.

TABLE 1: Bond Lengths, Bader Charges, and "Chemical Assignment" of the Different Oxygen Species[a]

	species	charge/e_0	O−O distance/Å	"chemical assignment"	energy/eV
	gaseous O_2	0	1.30	gaseous O_2	
I	molecular	−0.42	1.36	tilted superoxide atop one Mn^{surf}	−1.1
II	molecular	−0.65	1.43	horizontal peroxide atop one Mn^{surf}	−0.9
III	molecular	−0.69	1.41	horiz. peroxide atop O^{surf} = TS of O_2^- surface diffusion	−0.9
VII	molecular	−0.84	1.62	TS of dissociation without $V_O^{\cdot\cdot}$, atop O^{surf} and bridging two Mn^{surf}	−0.5
IV	molecular	−1.19	1.51	tilted peroxide in $V_O^{\cdot\cdot}$	−2.8
V	atom./molec.	−1.25	1.50	"vertical peroxide" in $V_O^{\cdot\cdot}$ = TS of O^- diffusion along surface	−2.4
VI	atomic	−0.62		2 O^- adsorbed atop Mn	2·(−1.1)
VIII	atomic	−1.19		oxygen ion in MnO_2[001] surface layer	2·(−3.3)
	atomic	−1.32		oxygen ion in LaO[001] surface layer	2·(−5.1)
	atomic	−1.25		bulk oxide ion	

[a] Experimental O−O bond lengths[29] for comparison: gaseous O_2 1.21 Å, hydrogen superoxide radical HO_2 1.33 Å, hydrogen peroxide H_2O_2 1.48 Å. TS = transition state. Energies ΔE^{DFT} (compare eq 4 and Figure 3; for adsorbate coverage of 12.5%) relative to gaseous O_2 (in triplet state) over surface containing two $V_O^{\cdot\cdot}$.

where

$$\Delta_f E^{DFT}_{bulk}(V_O^{\cdot\cdot}) = E_{bulk}(V_O^{\cdot\cdot}) + \frac{1}{2}E_{O_2} - E_{bulk} \quad (4)$$

is the formation energy of an oxygen vacancy with respect to the calculated energy $(1/2)E_{O_2}$ for an oxygen atom in the molecule, and

$$\Delta\mu_O(T, pO_2) = \mu_O(T, pO_2) - \frac{1}{2}E_{O_2} \quad (5)$$

The variation of oxygen chemical potential $\Delta\mu_O(T, pO_2)$ due to T, pO_2 comprises the experimental variation[28] and a correction term $\delta\mu_O^0$ (for details, see ref 21and eqs A.14−A.16 of the Supporting Information). Similarly, the vacancy formation energy for the surface vacancy can be represented as

$$\Delta_f G_{surf}(V_O^{\cdot\cdot}) = \Delta_f E^{DFT}_{surf}(V_O^{\cdot\cdot}) + \Delta\mu_O(T, pO_2) \quad (6)$$

where

$$\Delta_f E^{DFT}_{surf}(V_O^{\cdot\cdot}) = \frac{1}{2}(E_{slab}(2V_O^{\cdot\cdot}) + E_{O_2} - E_{slab}) \quad (7)$$

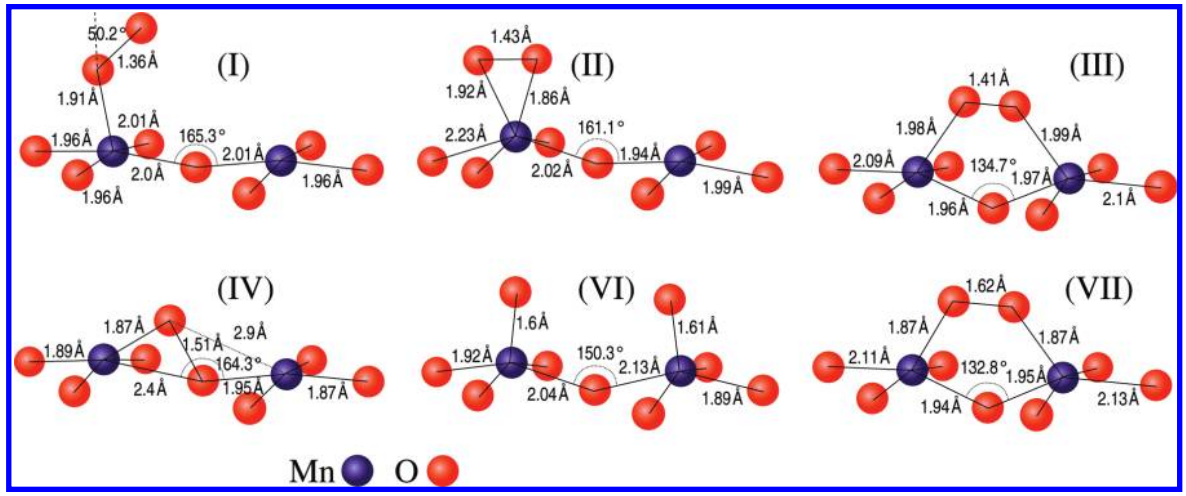

Figure 4. Geometry of some intermediates and transition states. **I** = adsorbed tilted superoxide, **II** = adsorbed horizontal peroxide, **III** = transition state of peroxide surface diffusion (horizontal peroxide atop O^{surf}), **IV** = tilted peroxide in $V_O^{\cdot\cdot}$, **VI** = two O^- atop Mn, **VII** = transition state of peroxide dissociation on the defect-free surface (for assignment see also Table 1).

Here we account for the symmetrical slab having a $V_O^{\cdot\cdot}$ at each side, and E_{slab} is the slab's total energy without defects. The Gibbs free energies of adsorption can be written analogously:

$$\Delta_{ads}G_{surf}(\text{ads. O}) = \Delta_{ads}E_{surf}^{DFT}(\text{ads. O}) - \Delta\mu_O \quad (8)$$

$$\Delta_{ads}E_{surf}^{DFT}(\text{ads. O}) = \frac{1}{2}(E_{slab}(2O) - E_{O_2} - E_{slab}) \quad (9)$$

$$\Delta_{ads}G_{surf}(\text{ads. O}_2) = \Delta_{ads}E_{surf}^{DFT}(O_2) - \Delta\mu_{O2} \quad (10)$$

$$\Delta_{ads}E_{surf}^{DFT}(\text{ads. O}_2) = \frac{1}{2}(E_{slab}(2O_2) - 2E_{O_2} - E_{slab}) \quad (11)$$

Again $\Delta\mu_O(T, pO_2)$ is given by eq 5, $\mu_{O_2} = 2\mu_O$, and we have to take account of two adsorbed O or O_2 on the symmetrical slab. The adsorption energy for atomic O species is given with respect to half an O_2 molecule. Adsorption energies $\Delta_{ads}E_{surf}^{DFT}$(ads. O), $\Delta_{ads}E_{surf}^{DFT}$(ads. O_2), and vacancy formation energies $\Delta_fE_{surf}^{DFT}(V_O^{\cdot\cdot})$ obtained for the MnO_2[001] termination as well as $\Delta_fE_{bulk}^{DFT}(V_O^{\cdot\cdot})$ are collected in Table 1. The assignments of oxygen species are based on charges and O−O bond length. The same energies are used to draw the energy diagram in Figure 3. In order to relate all relevant species to the same reference state, this was chosen to be a piece of surface containing two $V_O^{\cdot\cdot}$ and a gas phase O_2 molecule. While in drawing Figure 3 we neglect interactions between charged adsorbates or defects, in the further numerical calculations they are accounted for.[30,45]

Figure 3 is a very suitable graphical representation of the exchange between the gas phase and the crystal. For a given temperature and oxygen partial pressure, this diagram allows one to read the Gibbs reaction energy Δ_rG^0 of a process and thus to obtain its mass action constant. The left panel shows the energies of exemplary defect and adsorbate configurations relative to the reference state (all energies are given for an O_2 molecule). In the framework of the assumptions made in this study, the Gibbs free energy varies with T, pO_2 only due to dependence of oxygen chemical potential on these parameters in gaseous O_2 (i.e., only because the reference state in Figure 3 is sensitive to T and pO_2). The right panel shows the respective variation of chemical potential $\Delta\mu_O(T, pO_2)$ for gaseous oxygen. For given T, pO_2, the Gibbs energy of the reference state is found on the appropriate violet curve in the right panel while the T, pO_2-independent Gibbs energies of the final state (with adsorbed or incorporated oxygen) can be read from the left part. As an example let us discuss some processes under typical fuel cell conditions of $T = 1000$ K and $pO_2 = 1$ bar. The formation of molecular adsorbates (superoxide **I** = red arrow, and peroxide **II**) is endergonic by $\Delta_rG^0 \approx +2$ eV per O_2 since the entropy loss overcompensates the energy gain. Even the formation of adsorbed atomic O^- (species **VI**, green arrow) is still slightly endergonic by $\Delta_rG^0 \approx +0.5$ eV per O, which explains the low adsorbate coverage under SOFC conditions (see section 3.3). Only the oxygen incorporation (black arrow) is strongly exergonic by $\Delta_rG^0 \approx -1.7$ eV per O (i.e., the inverse process, oxygen vacancy formation, is endergonic by +1.7 eV). The barrier for O^- surface diffusion (2.0 eV) can be obtained from the comparison of state **VI** (O^- atop a Mn) with state **V** (O^- atop an oxide ion = transition state of O^- surface diffusion). Simultaneously state **V** also allows one to read the energy gain of 2.4 eV when an O_2 molecule is adsorbed into a surface vacancy to form a "vertical peroxide". For details of the geometry of some oxygen species, see Figure 4.

3.3. Quantitative Assessment of Adsorbate Coverage. Since the estimation of adsorbate coverage necessary for the kinetics discussion is not trivial, it is presented here in a separate section. As discussed in detail in ref 30, the formation of charged adsorbates (O_2^-, O_2^{2-}, O^-) and their mutual electrostatic interaction will lead to significant deviations from Langmuir's isotherm. For O_n^{j-} adsorbates the coverage θ reads

$$\theta_{O_n^{j-}} = K_{ad}(pO_2)^{n/2}\exp\left(-\frac{je_0\theta\chi_{max}}{kT}\right) \quad (12)$$

where j denotes adsorbate charge,[31] n the number of oxygen atoms it contains, and $K_{ad} = \exp(-\Delta G_{ad}^0/RT)$ the mass action constant of adsorption. χ_{max} is the surface potential drop built up in case of full coverage $\theta = 1$. In eq 12 it is assumed that the electronic charge carrier concentrations have a negligible pO_2 dependence.[32] The consequence of eq 12 is that the isotherms become flatter due to the electrostatic interaction when the coverage exceeds several percent. The coverage also depends

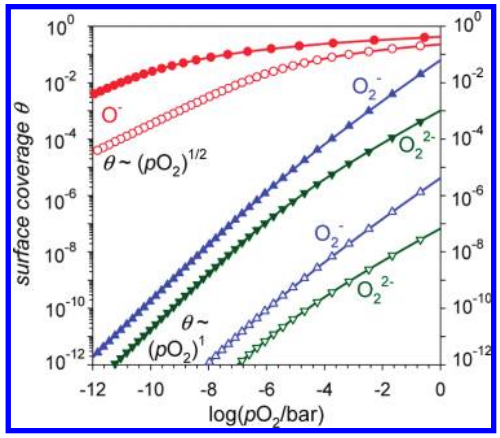

Figure 5. Oxygen adsorbate coverage at 1000 K, calculated from the DFT adsorption enthalpies ΔH^0_{ad} and estimated entropies $\Delta S^0_{ad} = -120$ J/(mol K) (solid symbols) or -200 J/(mol K) (open symbols). The levels of coverage for O_2^-, O_2^{2-} are obtained under the assumption that O^- (with $\Delta S^0_{ad} = -200$ J/(mol K)) is the species dominating the surface charge.

on which of the possible adsorbates prevails since θ and charge j of this dominant species have to be inserted in the exponent in eq 12.

For an actual calculation, adsorption enthalpies and entropies at elevated temperatures are required. Experimental adsorption enthalpies for O_2 on mixed conducting oxides are not available. Thus, adsorption enthalpies ΔH^0_{ad} (i.e., ΔE^{DFT} for the respective adsorption reaction) for O_2^-, O_2^{2-}, $2O^-$ are taken from the DFT results. The comparison of O^- adsorption enthalpies computed for 12.5% coverage (-1.13 eV) and 5% coverage (-1.23 eV) shows that these values contain electrostatic repulsion contributions. Taking this repulsion as being proportional to θ (cf. capacitor model of the surface[30]), this corresponds to a repulsive energy of 1.33 eV for full coverage. Extrapolation to infinitely low coverage yields $\Delta H^0_{ad}(O^-) = -1.3$ eV, and $\Delta H^0_{ad}(O_2^-) = -1.3$ eV, $\Delta H^0_{ad}(O_2^{2-}) = -1.1$ eV assuming a comparable repulsive energy. To be consistent with the repulsion contributions from the DFT results, χ_{max} in eq 12 has to be adjusted and was taken as 3 eV.[33]

Experimental O_2 adsorption entropies for mixed conducting oxides are also missing. Data for CO adsorption on different oxides (ZnO, SiO_2, Al_2O_3)[34] show that standard adsorption entropies ΔS^0_{ad} typically range between half of the standard entropy S^0 of the gaseous molecule and a value slightly below S^0.[35] A comparable adsorption entropy amounting to ≈70% of S_0 was obtained from the analysis of electrochemical oxygen reduction kinetics on Pt/YSZ, a process comprising dissociative oxygen adsorption.[36] Therefore we use $\Delta S^0_{ad} = -200$ and -120 J/(mol K) as limiting cases ($S^0(O_2, 1000\ K) = 245$ J/(mol K)[37]). For adsorbed O_2^- and O_2^{2-} the calculated rotation barriers of 0.04 and 0.13 eV are so low that rotation will be active. Additionally the O−O bond is weakened in O_2^- and O_2^{2-} compared to O_2 (where the O−O vibration already contributes to the O_2 heat capacity at 1000 K). These contributions justify the less negative $\Delta S^0_{ad} = -120$ J/(mol K) for O_2^-, O_2^{2-} in contrast to O^-.

The levels of adsorbate coverage resulting for $T = 1000$ K are shown in Figure 5.[38] The dominant species are adsorbed O^- ions because of their much larger ΔH^0_{ad}. In the flattened high pO_2 region, the different ΔS^0_{ad} values do not affect the resulting coverage very much. In this plateau also θ hardly varies with temperature ("apparent activation energies" being -0.05 to -0.13 eV). Since the coverage of the molecular adsorbates is smaller than for O^-, the surface charge created by O^- is employed for calculation of $\theta(O_2^-)$ and $\theta(O_2^{2-})$ leading to flattened O_2^- andO_2^{2-} isotherms as soon as $\theta(O^-)$ exceeds several percent. The resulting coverage lies in the range between ≈ 20% and 10^{-6} with the sequence $O^- > O_2^- > O_2^{2-}$.

3.4. Quantitative Assessment of Surface Oxygen Vacancy Concentration. Owing to the restrictions on computational effort of this study, we have to refer to experimental data for some quantities. Not $LaMnO_3$ but Sr-doped lanthanum manganate is applied as a SOFC cathode material, with a typical composition of $La_{0.8}Sr_{0.2}MnO_{3-\delta}$ (LSM). This acceptor doping by Sr'_{La} is predominantly compensated by electronic defects ($Mn^{\cdot}_{Mn}$, i.e. "Mn^{4+}") and only to a smaller degree by oxygen vacancy ($V^{\cdot\cdot}_O$) formation. Thus the $V^{\cdot\cdot}_O$ concentration in this LSM composition remains extremely small, typically in the range of $\delta \approx 10^{-9}$ at 973 K and $pO_2 = 1$ bar to $\delta \approx 10^{-7}$ at 1273 K (estimated from vacancy and tracer diffusion coefficients $D_{V_O^{\cdot\cdot}}$[39,40] and D^*[40]). While the bulk vacancy concentration is known for given pO_2 and T, $[V^{\cdot\cdot}_O]$ at the surface is not directly measurable. The DFT-calculated energy for the $V^{\cdot\cdot}_O$ formation reaction was found to be lower by 1.4 eV[12] in the surface layer compared to the bulk (a calculation for $LaMnO_3$ using different computer code and exchange-correlation functional yielded an energy lowering of 0.9 eV).[41] On the other hand, the $V^{\cdot\cdot}_O$ segregation energy in $(La_{0.75}Sr_{0.25})MnO_{3-\delta}$ amounts to only 0.5 eV.[42] Taking an average segregation energy of ≈1 eV, this enthalpy difference leads to an increase in the respective mass action constant K by 10^5 at 973 K. For $(La_{1-x}Sr_x)MnO_{3-\delta}$, this increase in $K = (pO_2)^{0.5}[V^{\cdot\cdot}_O][Mn^{3+}]^2/[Mn^{4+}]^2$ directly corresponds to an increase of $[V^{\cdot\cdot}_O]$ since the relative change of $[Mn^{4+}]$, $[Mn^{3+}]$ is small. Thus a significant increase of $[V^{\cdot\cdot}_O]$ at the surface to $[V^{\cdot\cdot}_O]^{surf} \approx 10^{-4}$ is expected.

For comparison the vacancy formation energy was also calculated for the LaO[001] termination and found to be more endothermic than bulk $V^{\cdot\cdot}_O$ formation by 0.8 eV. Thus the LaO[001] termination is not only disfavored by its higher surface Gibbs free energy, but in addition the concentration of surface oxygen vacancies (which are relevant for most of the discussed mechanisms) is strongly decreased relative to the MnO_2[001] termination. This further supports the decision to focus on the oxygen incorporation on the MnO_2[001] surface.

3.5. Relevant Reaction Steps.

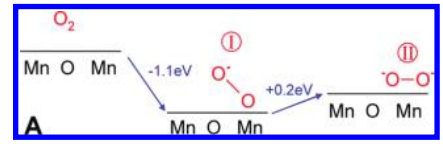

The reaction pathway leading from gaseous oxygen to oxide ions in the first layer of the $LaMnO_3$ crystal will be divided into several parts, which can be combined in different ways to the overall reaction. Scheme A covers the chemisorption of oxygen on a defect-free MnO_2 surface including electron transfers (Roman numbers indicate the oxygen species, see Table 1). Charge and bond length (Table 1) indicate that the tilted oxygen species **I** corresponds to a superoxide ion, O_2^-. This chemisorption step is exothermic by -0.9 eV. Species **II** can be regarded as a peroxide ion, O_2^{2-}, and is higher in energy by 0.2 eV. The calculated barriers for rotation about an axis perpendicular to the surface amount to 0.04 eV for O_2^- and 0.13 eV for O_2^{2-}.[43] As far as we know, there are no reliable experimental data on oxygen adsorbate coverage at close-to-operation conditions (elevated T, pO_2 > mbar) on $LaMnO_{3\pm\delta}$ or related perovskites available in literature for comparison.

Estimations based on the DFT results (section 3.3) indicate that the coverage of molecular adsorbates O_2^-,O_2^{2-} does not exceed a few percent. Since the superoxide **I** is lower in energy and thus higher in coverage, the following steps will be formulated starting from this adsorbate.

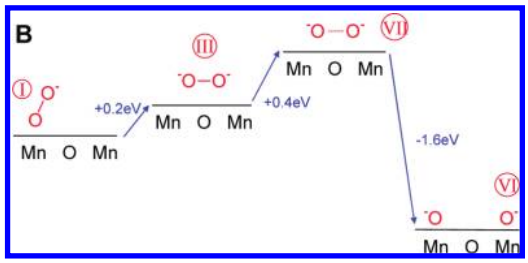

For the dissociation of superoxide **I**, two possibilities have to be considered. In the first (scheme B), the dissociation into two O^- ions occurs without interaction with other defects, which involves a barrier of 0.6 eV relative to species **I** although the final state **VI** is much lower in energy. In the transition state **VII**,[44] the O−O distance is elongated to 1.62 Å and the Mn−O_{ad} distance is similar to lattice Mn−O distances, but this bond is inclined by 37° relative to the surface normal (see Figure 4). In the final state **VI**, the two adsorbed O^- atop neighboring Mn experience a small mutual repulsion.[45]

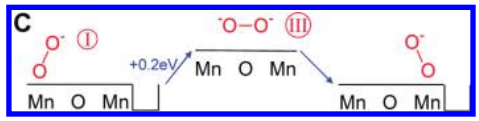

Alternatively, an oxygen vacancy $V_{\ddot{O}}$[46] could be involved in the dissociation. Before this can occur, the adsorbed superoxide and an oxygen vacancy have to approach each other (scheme C). The diffusion of adsorbed molecular oxygen along the surface has a barrier of 0.2 eV. The diffusion transition state **III**[47] can be viewed as a horizontal adsorbed peroxide connected to two neighboring Mn ions.

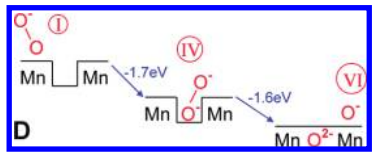

After encounter with a $V_{\ddot{O}}$, the superoxide is partly incorporated into the oxygen vacancy without barrier (scheme D). Species **IV** can be described as a tilted peroxide ion sticking in the oxygen vacancy. Due to this partial incorporation into the ionic solid, the total charge on the tilted peroxide **IV** is significantly more negative than of the surface adsorbate **I** (Table 1). The subsequent dissociation has a nonzero but very small barrier (i.e., species **IV** represents a shallow local energy minimum).[48]

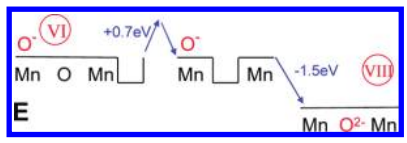

After the dissociation step we are left with adsorbed O^- (species **VI**) on the surface. Their incorporation requires the encounter of the O^- with a $V_{\ddot{O}}$. As shown in our previous study,[12] O^- diffusion along the MnO_2[001] surface has a high barrier of 2.0 eV[49] and the transition state (species **V** in Figure 2) can be regarded as a peroxide ion vertically inserted into a $V_{\ddot{O}}$. In contrast to O^- diffusion, the surface diffusion of a $V_{\ddot{O}}$ in the first crystal layer (i.e., MnO_2 plane) has a barrier of only 0.67 eV.[12] Thus the $V_{\ddot{O}}$ approaches O^- and not vice versa. Since additionally [$V_{\ddot{O}}$] is higher at the surface by a factor of 10^5 relative to the bulk, the supply of oxygen vacancies to oxygen adsorbates will primarily occur along the surface. In principle, the oxygen vacancy could also be supplied from the crystal's bulk. While the vacancies are supplied from a larger sampling zone (hemisphere extending into the bulk instead of circular area on the surface), the higher $V_{\ddot{O}}$ jump barrier in bulk $LaMnO_3$ (0.95 eV[12]) and the lower bulk vacancy concentration render this option less favorable.[50] The final incorporation step after the encounter occurs without barrier (the mutual O^-−$V_{\ddot{O}}$ electrostatic attraction leads to an energy gain of −0.7 eV[45] when the species are next-nearest neighbors).

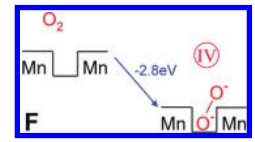

For situations with higher surface [$V_{\ddot{O}}$] and/or lower molecular oxygen adsorbate coverage (e.g., higher T, much lower pO_2, high Sr dopant concentration or Fe, Co instead of Mn), another mechanism shown in scheme F is worth considering: O_2 is chemisorbed from the gas phase right away into a $V_{\ddot{O}}$ leading directly to species **IV**. Dissociation and incorporation then continue as in schemes D and E.

3.6. Quantitative Assessment of Kinetic Parameters and Probable Mechanism. The most interesting (and difficult) part of our analysis is now to decide which combination of the different reaction steps in the mechanistic scheme results in the highest overall rate. Because of the lack of reliable data and in order to keep the treatment manageable, we use the standard attempt frequency of $\nu = 10^{13}$ s^{-1} and neglect entropy changes between reactant and transition states (unless otherwise stated). In the simplest approximation for elementary processes the reaction rates are given by

$$\prod_i [i] \cdot \nu \cdot e^{-\Delta E^{\neq}/kT} \qquad (13)$$

where $\prod_i[i]$ is the product of reactant concentration(s) and $\Delta E^{\neq}$ the barrier height. We also assume temperature-independent reaction barriers and enthalpies. (Please note that these approximations do not force the reaction mechanism to remain the same between 0 K and high T; the temperature- dependent levels of adsorbate coverage as well as the different barrier heights (i.e., different T dependences of various elementary reaction rates) still allow for a change from one pathway in the reaction network to another.) Actual numerical values are calculated for $pO_2 = 1$ bar and $T = 1000$ K and summarized in Table 2 and Figure 7. Since $(La_{1-x}Sr_x)MnO_{3-\delta}$ has a good electronic conductivity and its broad electronic bands offer a large range of electronic states, we assume that electronic charge transfers are fast compared to processes involving motion of particles and/or breaking of bonds.

Let us first consider mechanism M1 which starts with chemisorption directly into $V_{\ddot{O}}$ (scheme F above). This process

TABLE 2: Overall Oxygen Incorporation Rates for the Different Oxygen Incorporation Pathways (T = 1000 K, pO_2 = 1 bar, $[V_O^{\cdot\cdot}]^{surf} = 10^{-4}$)[a]

mechanism	rate per s per unit cell (16 Å^2)	rate-determining step rds	activation energy E_a, pO_2 dependence[b]
M1 F−D−E	$[V_O^{\cdot\cdot}]^{surf}\cdot 2\cdot 10^7$	adsorption of O_2 into surface-$V_O^{\cdot\cdot}$	3.3 eV $(pO_2)^{0.66}$
M2 A−B−E	$\theta(O_2^{i-})\cdot 3\cdot 10^9$	dissociation of O_2^{i-} without $V_O^{\cdot\cdot}$	0.6 to −0.5 eV $(pO_2)^0-(pO_2)^1$
M2′ A−B−E	$[V_O^{\cdot\cdot}]^{surf}\cdot\theta(O^-)\cdot 10^{11}$	approach of $V_O^{\cdot\cdot}$ to O^-	4.0−2.7 eV $p(O_2)^{-0.34}-(pO_2)^{0.16}$
M3 A−C−D−E	$[V_O^{\cdot\cdot}]^{surf}\cdot\theta(O_2^{i-})\cdot 10^{12}$	approach of O_2^{i-} to $V_O^{\cdot\cdot}$	3.5−2.2 eV $p(O_2)^{-0.34}-(pO_2)^{0.66}$
M3′ A−C−D−E	$[V_O^{\cdot\cdot}]^{surf}\cdot\theta(O^-)\cdot 10^{11}$	approach of $V_O^{\cdot\cdot}$ to O^-	4.0−2.7 eV $p(O_2)^{-0.34}-(pO_2)^{0.16}$

[a] The experimental activation energy and pO_2 dependence for $La_{1-x}Sr_xMnO_{3-\delta}$ are E_a = 1.3−2.4 eV[57,58] and exchange rate ∝ $(pO_2)^{0.49}$.[10] [b] The first entry for E_a, pO_2 dependence refers to the limit of high adsorbate coverage, the second entry to low coverage.

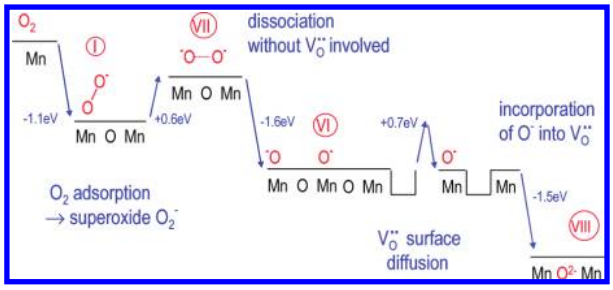

Figure 6. Schematic diagram of the energetics and steps in oxygen reduction mechanism M2.

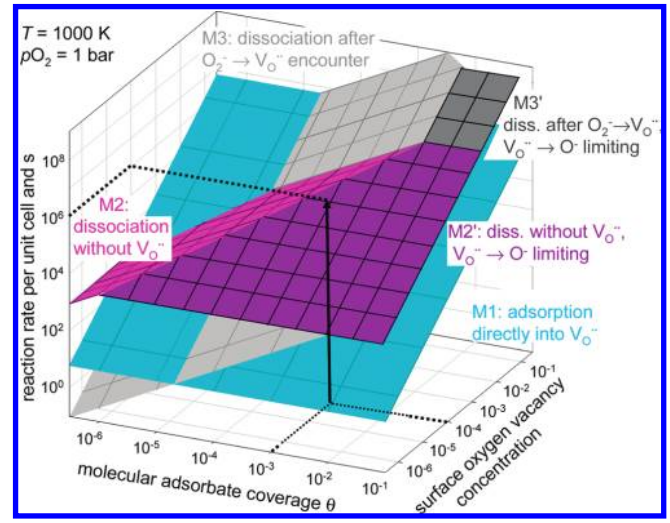

Figure 7. Variation of the oxygen exchange rates on MnO_2[001]-terminated $La_{1-x}Sr_xMnO_{3-\delta}$ with surface oxygen vacancy concentration $[V_O^{\cdot\cdot}]^{surf}$ and coverage of molecular adsorbates (O_2^- or O_2^{2-}) at T = 1000 K, pO_2 = 1 bar, $\theta(O^-)$ = 0.1. The differently colored planes refer to the different mechanisms as discussed in the text. For typical $La_{1-x}Sr_xMnO_{3-\delta}$ parameters $[V_O^{\cdot\cdot}]^{surf} = 10^{-4}$ and $\theta(O_2^-) = 0.001$, oxygen incorporation is predicted to occur by mechanism M2′; for lower pO_2 and thus lower $\theta(O_2^-)$ a switchover to M2 is expected.

is essentially equivalent to the situation that the oxygen molecule first adsorbs on a Mn neighboring $V_O^{\cdot\cdot}$ because the transformation to species **IV** occurs without barrier (step D1). As calculated from ideal gas theory[51] about $8\cdot 10^6$ O_2 molecules per unit cell area (≈16 Å^2) per second hit the surface if one assumes a sticking probability of 0.1.[51] An additional constraint is that the oxygen molecule has to hit a $V_O^{\cdot\cdot}$ (or one of the neighboring two Mn ions). For a surface vacancy concentration of 10^{-4}, this results in a rate of 80 chemisorbed oxygen molecules per unit cell per second. The subsequent dissociation of species **IV** in step D2 has a very small barrier and is faster. The $V_O^{\cdot\cdot}-O^-$ approach in step E1 is also faster (see Supporting Information), and the final incorporation in step E2 is barrier-free. Therefore this is also the overall reaction rate (only for the improbable case of $\theta(O^-)$ being lower than $\approx 10^{-5}$ the final part E in this sequence would become limiting with a rate of $[V_O^{\cdot\cdot}]^{surf}\cdot\theta(O^-)\cdot 10^{11}$ s^{-1} at 1000 K).

The next mechanism M2 with the overall reaction path A−B−E is oxygen chemisorption and dissociation without participation of oxygen vacancies (see Figure 6). The chemisorption up to the formation of superoxide **I** and peroxide species **II** is fast[51] relative to the following dissociation process B since here no surface vacancies are required. Thus equilibrium O_2^- concentration can be assumed, being $\theta \approx 10^{-3}$ (see section 3.3). With the standard attempt frequency of 10^{13} s^{-1} and a factor of 0.5 taking account of the required orientation of the tilted superoxide, the barrier of 0.6 eV for the dissociation (scheme B) results in a rate of $\approx 3\cdot 10^6$ per surface unit cell (16 Å^2) per second at 1000 K. For the final incorporation a surface vacancy approaches the adsorbed O^- with a rate of $[V_O^{\cdot\cdot}]^{surf}\cdot\theta(O^-)\cdot 10^{11}$ s^{-1} (see Supporting Information) while the incorporation occurs without barrier and much faster (scheme E). Thus for typical LSM parameters $[V_O^{\cdot\cdot}]^{surf} = 10^{-4}$ and $\theta(O^-) = 0.1$, the $V_O^{\cdot\cdot}-O^-$ approach limits the overall rate (mechanism M2′). This change of the rate-determining step, in particular for higher coverage of molecular oxygen adsorbates $\theta(O_2^{i-})$, is illustrated in Figure 7 by the transition from the magenta to the violet plane.

The final mechanism M3 (path A−C−D−E) comprises chemisorption without involving $V_O^{\cdot\cdot}$, but with dissociation being facilitated by interaction with $V_O^{\cdot\cdot}$. As discussed for mechanism M2, the formation of superoxide **I** and peroxide species **II** on the defect-free surface is fast and equilibrium concentrations can be inserted. Then the molecular oxygen adsorbate approaches the surface vacancy (scheme C). Due to the low diffusion barrier of 0.2 eV, the rate of $[V_O^{\cdot\cdot}]^{surf}\cdot\theta(O_2^{i-})\cdot 10^{12}$ s^{-1} is significantly higher than the $V_O^{\cdot\cdot}-O^-$ approach (see Supporting Information). The further steps in scheme D up to and including the dissociation occur almost without any barrier. Thus for low O_2^{i-} coverage ($\theta(O_2^{i-}) < 0.0003$) the approach of O_2^{i-} to $V_O^{\cdot\cdot}$ is rate-determining (M3), while for high coverage of molecular oxygen adsorbates $\theta(O_2^{i-})$ the $V_O^{\cdot\cdot}-O^-$ approach (scheme E) can become limiting as shown in Figure 7 by the transition to the dark gray plane (mechanism M3′).

The summary given in Table 2 and Figure 7 shows that for typical $La_{1-x}Sr_xMnO_{3-\delta}$ parameters $[V_O^{\cdot\cdot}]^{surf} = 10^{-4}$, $\theta(O_2^{i-}) = 10^{-3}$, and $\theta(O^-) = 0.1$, oxygen incorporation by mechanism M2′ (i.e., by the approach of a $V_O^{\cdot\cdot}$ to adsorbed O^- being limiting) is predicted to have the fastest overall rate.[44] Keeping the uncertainties in the calculated barriers and the necessary simplifications/assumptions in mind, a crossover to mechanism M2 (dissociation without $V_O^{\cdot\cdot}$ assistance, the actual dissociation

being limiting) upon a slight change of conditions cannot be ruled out. The next fastest mechanism is the dissociation after encounter of O_2^{i-} and $V_O^{\cdot\cdot}$ (M3), and this mechanism will become dominant for materials with higher surface vacancy concentration. This comparison also illustrates that steps of very different nature can become rate-determining: thermally activated surface diffusion of adsorbates and vacancies, dissociation of molecular oxygen adsorbates with a reaction barrier, or in the case of M1 even adsorption from the gas phase.

Finally let us compare the DFT-based results with experimental data. The overall DFT oxygen incorporation energy into a surface vacancy is −3.25 eV per oxygen atom (see $\Delta_r G^0$ for final state **VIII** in Figure 3). In order to compare with experimental bulk data, the vacancy surface segregation energy of about 1 eV has to be added. The resulting value of ≈−4.2 eV is about 1 eV more exothermic[52] than the experimental data ($2Mn_{Mn}^x + V_O^{\cdot\cdot} + 0.5O_2 \rightleftharpoons 2Mn_{Mn}^{\cdot} + O_O^x$: $\Delta H_{ox}^0 = -3.1$ eV for $La_{0.8}Sr_{0.2}MnO_{3-\delta}$[53] and $\Delta H_{ox}^0 = -2.3$ to (−3.5) eV for $La_{0.9}Sr_{0.1}MnO_{3-\delta}$ and $La_{0.8}Sr_{0.2}MnO_{3-\delta}$;[54] from the relation between $D_{V_O^{\cdot\cdot}}$ and D^* for $La_{0.5}Sr_{0.5}MnO_{3-\delta}$[40] a similar value of $\Delta H_{ox}^0 = -2.8$ eV can be estimated[55]). From the microelectrode study on $La_{0.74}Sr_{0.18}MnO_{3-\delta}$, [10] an effective rate constant $k^q = 2\cdot10^{-9}$ cm/s is obtained (extrapolated to $pO_2 = 1$ bar, 1000 K) which corresponds to an exchange rate of about 0.2 per unit cell per second[56] (the experimental error bar is about one order of magnitude). When comparing with the theoretical values, one has to keep in mind the uncertainties in adsorbate coverage and surface vacancy concentration as well as the fact that an error in an energy barrier (or in the energy level and thus concentration of an intermediate species) of 0.2 eV changes the rate by a factor of 10. This is an important point since the calculated ΔH_{ox}^0 is by ≈1 eV too exothermic compared to the experiment, which leads to an overestimation of the stabilization of intermediates (i.e., too high concentrations) and too low barriers. For the calculation of adsorbate coverage in section 3.3, the parameters (use of Bader charges instead of formal adsorbate charges; lower value for χ_{max}[33]) are chosen such that they rather underestimate adsorbate repulsion and thus overestimate levels of coverage. Also the difference between the real and ideal surface structure and composition (see Introduction) has to be taken into account. The DFT overestimation of ΔH_{ox}^0 by ≈1 eV also affects directly all activation energies which have a contribution from $[V_O^{\cdot\cdot}]^{surf}$ (mechanisms M1, M2′, M3, M3′), but an indirect effect on M2 by overestimated adsorption enthalpies may also occur.

The experimental pO_2 dependence of the surface rate constant k^q of $La_{0.74}Sr_{0.18}MnO_{3-\delta}$ is $(pO_2)^{0.49}$ (ref 10, no activation energy was measured). For $La_{0.8}Sr_{0.2}MnO_{3-\delta}$ and $La_{0.5}Sr_{0.5}MnO_{3-\delta}$, activation energies of k^* in the range of 1.3−2.4 eV[57,58] and of k^q in the range of 1.7−1.9 eV[59] were obtained.

The predicted activation energies (comprising reaction barrier as well as contributions from T-dependent defect concentrations or adsorbate coverage) and pO_2 dependences for the different mechanisms are also summarized in Table 2. For mechanism M1 (rds = adsorption of O_2 directly into $V_O^{\cdot\cdot}$), the number of successful impacts is $\propto pO_2$. Assuming $[V_O^{\cdot\cdot}]^{surf} \propto [V_O^{\cdot\cdot}]^{bulk}$ and taking the experimental dependence $[V_O^{\cdot\cdot}]^{bulk} \propto (pO_2)^{-0.34}$ (ref 60), the exchange rate becomes $\propto (pO_2)^{0.66}$. E_a is determined mainly by the T dependence of $[V_O^{\cdot\cdot}]^{surf}$ of about 3.25 eV (assuming a low T dependence of the electronic charge carrier concentration) since the T dependence of the O_2 impact frequency is weak.[51]

For mechanism M2 the rds is dissociation without involvement of $V_O^{\cdot\cdot}$ starting from O_2^-. Depending on the actual conditions the adsorption isotherm will yield either $\theta(O_2^-) \propto (pO_2)^1$ or a smaller exponent if the coverage approaches the saturation plateau. This is also the pO_2 dependence of the exchange rate (electronic charge carrier concentrations are assumed to be approximately pO_2-independent). The activation energy results from the dissociation barrier of 0.6 eV and the negative contribution from the adsortion enthalpy (as long as the isotherm has not yet reached the approximately T-independent saturation plateau) which can even lead to a negative effective E_a.[61] If instead of the dissociation the approach of $V_O^{\cdot\cdot}$ to adsorbed O^- becomes limiting (mechanism M2′), the overall activation energy is the sum of the surface diffusion barrier of 0.7 eV, the T dependence of $[V_O^{\cdot\cdot}]^{surf}$ contributing 3.25 eV, and a potential negative contribution from the O^- adsorption enthalpy (depending on the actual position on the adsorption isotherm). The pO_2 dependence results from $[V_O^{\cdot\cdot}]^{surf} \propto (pO_2)^{-0.34}$ (see above) and $\theta(O^-) \propto (pO_2)^0$ to $(pO_2)^{1/2}$ depending on the actual position on the isotherm. The typical $[V_O^{\cdot\cdot}]^{surf}$, $\theta(O_2^-)$, and $\theta(O^-)$ for $La_{1-x}Sr_xMnO_{3-\delta}$ locate the mechanism close to the boundary between M2 and M2′; therefore, a decrease of pO_2 and thus of $\theta(O_2^-)$ can lead to a smooth switchover into the pO_2-dependent M2 regime. Such an intermediate situation reasonably agrees with the experimentally observed pO_2 dependence of $k^q \propto (pO_2)^{0.49}$ (measured in a limited pO_2 range between $3\cdot10^{-5}$ and $3\cdot10^{-2}$ bar) and activation energy of ≈2 eV.

In mechanism M3 the approach of O_2^- to $V_O^{\cdot\cdot}$ is limiting, and thus the exchange rate is $\propto D_{O_2^-}\cdot\theta(O_2^-)\cdot[V_O^{\cdot\cdot}]^{surf}$ ($D_{O_2^-}$ = diffusion coefficient of O_2^- parallel to the surface). Depending on the actual regime of the adsorption isotherm, $\theta(O_2^-) \propto (pO_2)^0$ to $(pO_2)^1$. Assuming again $[V_O^{\cdot\cdot}]^{surf} \propto (pO_2)^{-0.34}$ leads to an exchange rate $\propto (pO_2)^{-0.34}$ to $(pO_2)^{0.66}$. E_a is mainly determined by the diffusion barrier of $D_{O_2^-}$ (=0.2 eV) plus the "activation energy" of $[V_O^{\cdot\cdot}]^{surf}$ of 3.25 eV resulting in about 3.5 eV, plus a potential negative contribution from the O_2^- adsorption enthalpy. In the case of O^- incorporation becoming limiting (mechanism M3′), E_a and pO_2 dependence are the same as for M2′.

Unfortunately the predicted pO_2 dependence and E_a ranges of the different mechanisms overlap strongly. Thus though the predictions from the most probable mechanisms M2/M2′ are in reasonable agreement with the experimental values, the comparison does not really yield an independent confirmation that M2/M2′ is the correct mechanism. Despite some residual uncertainty, this study yields significant information about important aspects of oxygen incorporation kinetics (e.g., the importance of transport steps such as $V_O^{\cdot\cdot}$ surface diffusion) which are not available from experiments alone.

4. Summary and Conclusion

Based on DFT calculations, the kinetic parameters for realistic SOFC operating conditions ($pO_2 = 1$ bar, $T = 1000$ K) have been assessed. The necessary approximations for deducing reaction rates at elevated temperature from 0 K DFT results have been discussed. The estimated reaction rates of various elementary steps allowed us to draw conclusions on the most favorable oxygen incorporation pathway on the MnO_2[001] termination of $(La_{1-x}Sr_x)MnO_{3-\delta}$. Its rate-determining step is predicted to be the encounter of a surface oxygen vacancy and adsorbed O^- by thermally activated diffusion of the vacancy along the surface. Thus, both a high surface vacancy concentration, reducing the required diffusion length, and a high mobility are beneficial for obtaining a high reaction rate. The obtained activation energy and pO_2 dependence are in reasonable agreement with experimental data when we consider a change in the rate-determining step to the actual dissociation of

molecular oxygen species for lower pO_2. Notwithstanding the limitations and approximations made in this study, the DFT calculations yield valuable mechanistic insight, e.g., concerning the importance of surface $V_{\ddot{O}}$ concentration and mobility, beyond experimental findings. The mechanism on other surface terminations, other cation compositions, or even non-perovskite-type surface structures remains to be studied in detail (although the much lower $V_{\ddot{O}}$ concentration on the LaO termination already points toward a less favorable oxygen incorporation process). Despite the necessary assumptions and simplifications, this study demonstrates the complex nature of the oxygen incorporation reaction mechanism where surface transport steps (on a rather short length scale) as well as actual reactions (dissociation of molecular adsorbates) can become limiting.

Acknowledgment. We thank V. E. Alexandrov (MPI Stuttgart, Germany), M. M. Kuklja (University of Maryland), and S. Piskunov (University of Essen, Germany) for valuable discussions as well as U. Traub (MPI Stuttgart) for technical support. This work is supported in part by the National Science Foundation. Any appearances of findings, conclusions, or recommendations expressed in this material are those of the authors and do not necessarily reflect views of NSF.

Supporting Information Available: Identification of the most stable $LaMnO_3$ terminations. This material is available free of charge via the Internet at http://pubs.acs.org.

References and Notes

(1) Merkle, R.; Maier, J. *Angew. Chem., Int. Ed.* **2008**, *47*, 2.

(2) Horita, T.; Yamaji, K.; Sakai, N.; Yokokawa, H.; Kawada, T.; Kato, T. *Solid State Ionics* **2000**, *127*, 55.

(3) Kawada, T.; Suzuki, J.; Sase, M.; Kaimai, A.; Yashiro, K.; Nigara, Y.; Mizusaki, J.; Kawamura, K.; Yugami, H. *J. Electrochem. Soc.* **2002**, *149*, E252.

(4) Koep, E.; Mebane, D. S.; Das, R.; Compson, C.; Liu, M. L. *Electrochem. Solid State Lett.* **2005**, *8*, A592.

(5) Bieberle-Hutter, A.; Sogaard, M.; Tuller, H. L. *Solid State Ionics* **2006**, *177*, 1969.

(6) Fleig, J. *Solid State Ionics* **2003**, *161*, 279.

(7) Baumann, F. S.; Fleig, J.; Habermeier, H.-U.; Maier, J. *Solid State Ionics* **2006**, *177*, 1071.

(8) Merkle, R.; Maier, J. *Top. Catal.* **2006**, *38*, 141.

(9) Mizusaki, J.; Saito, T.; Tagawa, H. *J. Electrochem. Soc.* **1996**, *143*, 3065.

(10) Fleig, J.; Kim, H.-R.; Jamnik, J.; Maier, J. *Fuel Cells* **2008**, *8*, 330.

(11) Fleig, J. *J. Power Sources* **2002**, *105*, 128.

(12) Kotomin, E. A.; Mastrikov, Y. A.; Heifets, E.; Maier, J. *Phys. Chem. Chem. Phys.* **2008**, *10*, 4644.

(13) Merkle, R.; Mastrikov, Y. A.; Heifets, E.; Kotomin, E. A.; Kuklja, M. M.; Maier, J. *ECS Trans.* **2009**, *25*, 2753.

(14) Choi, Y. M.; Lin, M. C.; Liu, M. L. *Angew. Chem., Int. Ed.* **2007**, *46*, 7214.

(15) Choi, Y. M.; Mebane, D. S.; Lin, M. C.; Liu, M. L. *Chem. Mater.* **2007**, *19*, 1690.

(16) Choi, Y. M.; Lynch, D. E.; Lin, M. C.; Liu, M. L. *J. Phys. Chem. C* **2009**, *113*, 7290.

(17) Kresse, G.; Furthmüller, J. *VASP, the Guide*; University of Vienna: Austria, 2003; Kresse, G.; Hafner, J. *Phys. Rev. B* **1993**, *47*, 558. Kresse, G.; Furthmüller, J. *Phys. Rev B* **1996**, *54*, 11169.

(18) Bloechl, P. E. *Phys. Rev. B* **1994**, *50*, 17953. Kresse, G.; Joubert, D. *Phys. Rev. B* **1999**, *59*, 1758.

(19) Perdew, J. P.; Chevary, J. A.; Vosko, S. H.; Jackson, K. A.; Pederson, M. R.; Singh, D. J.; Fiolhais, C. *Phys. Rev. B* **1992**, *46*, 6671.

(20) Monkhorst, H. J.; Pack, J. D. *Phys. Rev. B* **1976**, *13*, 5188.

(21) Mastrikov, Y. A.; Heifets, E.; Kotomin, E. A.; Maier, J. *Surf. Sci.* **2009**, *603*, 326.

(22) Evarestov, R. A.; Kotomin, E. A.; Mastrikov, Yu.; Gryaznov, D.; Heifets, E.; Maier, J. *Phys. Rev. B* **2005**, *72*, 214411.

(23) Henkelman, G.; Uberuaga, B. P.; Jónsson, H. *J. Chem. Phys.* **2000**, *113*, 9901. Henkelman, G.; Johannesson, G.; Jónsson, H. In *Progress on Theoretical Chemistry and Physics*; Schwartz, S. D., Ed.; Kluwer: New York, 2000.

(24) Henkelman, G.; Arnaldsson, A.; Jónsson, H. *Comput. Mater. Sci.* **2006**, *36*, 354.

(25) Bottin, F.; Finocchi, F.; Noguera, C. *Phys. Rev. B* **2003**, *68*, 035418.

(26) Reuter, K.; Scheffler, M. *Phys. Rev. B* **2001**, *65*, 035406.

(27) Oganov, A. R.; Price, G. D. *J. Chem. Phys.* **2005**, *122*, 124501.

(28) Chase, M. W. *NIST-JANAF Thermochemical Tables*; American Chemical Society: Washington DC, 1998.

(29) *NIST Computational Chemistry Comparison and Benchmark Database*, 14th ed.; American Chemical Society: Washington DC, 2006.

(30) Fleig, J.; Merkle, R.; Maier, J. *Phys. Chem. Chem. Phys.* **2007**, *9*, 2713. In this article the deviation from Langmuir's isotherm is quantified with a plate capacitor model (double layer of negatively charged adsorbates and compensating positive charges in the first materials layer). The situation can as well be regarded as mutual repulsion of the charged adsorbates.

(31) While integer formal charges of -1 and -2 were applied in ref 30, here we use the Bader charges of the adsorbates. If the adsorbate charge is underestimated by the Bader charge, this will lead to an overestimated coverage. $\theta(O^-)$ reaches the plateau for large pO_2 in Figure 4 and is not very sensitive to modifications of the actual charge. $\theta(O_2^-)$ and $\theta(O_2^{2-})$ decrease by up to two orders of magnitude in the region of high $\theta(O^-)$ if the formal charges are used.

(32) The levels of adsorbate coverage are calculated here for the case of approximately constant hole and electron concentration as given in ref 30. This condition is fulfilled under the conditions considered here (high pO_2); see, e.g.: van Hassel, B. A.; Kawada, T.; Sakai, N.; Yokokawa, H.; Dokiya, M.; Bouwmeester, H. J. M. *Solid State Ionics* **1993**, *66*, 295. Poulsen, F. W. *Solid State Ionics* **2000**, *129*, 145, and references therein.

(33) In ref 30, a value of $\chi_{max} = 10$ V was estimated based on one adsorbate molecule per surface elementary cell, surface−adsorbate distance of 1 Å, and $\epsilon_r = 1$ (vacuum). Here we use $\chi_{max} = 3$ V which can be justified by a larger relative dielectric constant ϵ_r.

(34) Garrone, E.; Ghiotti, G.; Giamello, E.; Fubini, B. *J. Chem. Soc., Faraay. Trans.* **1981**, *77*, 2613.

(35) Thus, the construction in the right part of Figure 3 represents only a first approximation since it assumes that upon adsorption the translational, rotational, and vibrational degrees of freedom from the gaseous O_2 are completely lost.

(36) Bronin, D. I.; Yaroslavtsev, I. Y.; Näfe, H.; Aldinger, F. *Electrochim. Acta* **2004**, *49*, 2435, and references therein.

(37) Barin, I.; Knacke, O. *Thermochemical Properties of Inorganic Substances*; Springer: Berlin, Germany, 1973.

(38) Please note that the levels of coverage calculated here are equilibrium values. While they will be valid also for small deviations from equilibrium (e.g., in ac impedance measurements with sufficiently small excitation amplitude), their values will deviate under nonequilibrium conditions (large dc bias) and in this case also will depend on the reaction mechanism and its rate-determining step, see: Fleig, J. *Phys. Chem. Chem. Phys.* **2005**, *7*, 2027.

(39) Ishigaki, T.; Yamauchi, S.; Kishio, K.; Mizusaki, J.; Fueki, K. *J. Solid State Chem.* **1988**, *73*, 179.

(40) De Souza, R. A.; Kilner, J. A. *Solid State Ionics* **1998**, *106*, 175.

(41) Piskunov, S. Private communication. Calculation with CRYSTAL06 code (Torino, Italy, 2006) using the B3LYP hybrid density functional; see ref 42.

(42) Piskunov, S.; Heifets, E.; Jacob, T.; Kotomin, E. A.; Ellis, D. E.; Spohr, E. *Phys. Rev. B* **2008**, *78*, 121406.

(43) Since the structure of the $LaMnO_3$ is orthorhombic, the energies of orientations differing by 90° rotation differ by a nonzero but negligible small amount of 0.02−0.03 eV. The energy minimum for O_2^{2-} corresponds to an orientation with the O−O bond parallel to the Mn−O bonds.

(44) After submission of our previous paper,[13] we further refined the location of the transition state **VII** by stepwise manually increasing the O−O bond length and then fully optimizing all other parameters, which leads to a significant energy lowering. For $La_{1-x}Sr_xMnO_{3-\delta}$ the mechanism with the fastest overall rate turns out to be not M3 as stated there but M2 or M2′. Nevertheless, the conclusion that for $La_{1-x}Sr_xCo_{1-y}Fe_yO_{3-\delta}$ (with significantly higher $[V_{\ddot{O}}]$) oxygen incorporation proceeds by mechanism M3 and is faster than for $La_{1-x}Sr_xMnO_{3-\delta}$ remains valid.

(45) There are several repulsive and attractive interactions between charged adsorbates and surface $V_{\ddot{O}}$. The repulsion between the two O^- adsorbed on neighboring Mn (final state of section B) is + 0.05 eV; this small value has no significant effect on barriers. The attraction of O^- adsorbed on Mn and $V_{\ddot{O}}$ is 0.7 eV, and for $V_{\ddot{O}}-O_2^-$ and $V_{\ddot{O}}-O_2^{2-}$ similar values are expected. Attractive interactions of this magnitude might lower reaction barriers, especially for the last step of the mutual approach where the strongest change of attraction energy is expected. On the other hand, if the approach comprises many jumps at larges distances, the acceleration of the last jump will hardly change the rate. The attraction energy of 0.7 eV may seem to be rather high, but it is still within the range of defect interactions of 0.4−0.9 eV observed in the bulk of $BaZrO_3$ between M'_{Zr} dopants and $V_{\ddot{O}}$ given in Sundell, P. G.; Björketun, M. E.; Wahnström, G. *Phys. Rev. B* **2006**, *73*, 104112.

(46) When we denote the (surface) oxygen vacancy as $V_{\ddot{O}}$, this is not intended to make a strict statement about its charge state. Since the bonding

has a significant degree of covalency, neither the charge of the oxide ion nor of the oxygen vacancy is exactly 2− or 2+.

(47) Energy, charge, and geometry of transition state **III** were determined by the nudged elastic band method. Note that in the first attempts to locate transition state **III** the lowest-energy configuration was not reached. Thus the conclusions drawn from the energy of this transition state in our previous publication ref 13 are now refined. In the $V_O^{\cdot\cdot}-O_2^-$ encounter for $La_{1-x}Sr_xMnO_{3-\delta}$, the diffusion of O_2^- is much faster than that of $V_O^{\cdot\cdot}$, and the contribution of the respective barrier to the overall activation energy is lowered accordingly. Nevertheless, for different materials such as $Ba_{0.5}Sr_{0.5}Co_{0.8}Fe_{0.2}O_{3-\delta}$ with higher $D_{V_O}^{surf}$ and larger lattice constant regarding the O_2^- diffusion, the conclusion drawn in ref 13 that it is rather the $V_O^{\cdot\cdot}$ which approaches the O_2^- may still be valid.

(48) A nudged elastic band calculation with moderate resolution could not detect a barrier for step D2; thus, the barrier is definitely below 0.3 eV. Therefore, it does not significantly impede the kinetics.

(49) This transition state **V** (=peroxide ion vertically inserted in a $V_O^{\cdot\cdot} = O^-$ adsorbed on top of an oxide ion) is higher in energy than gaseous O_2 over the perfect $LaMnO_3$ surface. Nevertheless, desorption cannot occur as atomic oxygen but requires formation of the tilted peroxide **IV**, and its desorption then creates a $V_O^{\cdot\cdot}$ which costs 0.9 + 1.5 eV = 2.4 eV. This process is even less favorable than direct O^- diffusion.

(50) Of course the surface $V_O^{\cdot\cdot}$ have to be replenished from the underlying bulk, but in this process it is sufficient if a $V_O^{\cdot\cdot}$ arrives somewhere in the surface layer; it does not have to meet an adsorbed oxygen species directly. Thus this can occur faster than the steps of the surface reaction. At high pO_2 or for thick films, the transport through the complete (La, Sr)$MnO_{3-\delta}$ film can become limiting.[10]

(51) Estimation of chemisorption kinetics: according to ideal gas theory, the number of impacts on a wall for $pO_2 = 1$ bar at 1000 K is $N_A p/(2\pi RTM)^{1/2} = 2\cdot10^8$ per $LaMnO_3$ surface unit cell (≈16 Å^2) and second (M = molar mass). Experimental data for sticking coefficients on mixed conducting oxides are not available, but they should be comparably high since the SOFC cathode materials can easily transfer electrons to form O_2^- and O_2^{2-} (note that at least the first charge transfer is fast even on a semiconductor such as SnO_2, since this charge transfer generates the sensor signal in Taguchi-type gas sensors typically operated at 473−573 K). We adopt a value of 0.1 which was found to be the upper limit for strong oxygen chemisorption on Pt; see: Mitterdorfer, A.; Gauckler, L. J. *Solid State Ionics* **1999**, *117*, 203; *Solid State Ionics* **1999**, *120*, 211.

(52) The overestimation of the oxidation enthalpy can to a certain degree be traced back to the "DFT error" of 0.7 eV per O. While this correction would significantly improve the value of the overall oxidation enthalpy, it is difficult to apply it in a consistent way to all other intermediates and transitions states which occur between the oxidized (perfect) surface and the oxygen-deficient surface. In order not to distort the energy profile arbitrarily, we refrain from applying this correction for the data used as the basis of the kinetic treatment.

(53) Nowotny, J.; Rekas, M. *J. Am. Ceram. Soc.* **1998**, *81*, 67.

(54) Mebane, D. S.; Liu, Y.; Liu, M. L. *Solid State Ionics* **2008**, *178*, 1950.

(55) Merkle, R.; Maier, J.; Bouwmeester, H. J. M. *Angew. Chem., Int. Ed.* **2004**, *43*, 5069.

(56) $k^q = \Delta x \cdot \boldsymbol{R}_0/c_O = \boldsymbol{R}_0'/c_O$, where $c_O = 5\cdot10^{22}$ cm^{-3} is the oxygen concentration in the solid and $\boldsymbol{R}_0'$ is the area-normalized oxygen exchange rate; see, e.g.: Maier, J. *Solid State Ionics* **1998**, *112*, 197.

(57) De Souza, R. A.; Kilner, J. A. *Solid State Ionics* **1999**, *126*, 153.

(58) De Souza, R. A.; Kilner, J. A.; Walker, J. F. *Mater. Lett.* **2000**, *43*, 43.

(59) la O', G. J.; Yildiz, B.; McEuen, S.; Shao-Horn, Y. *J. Electrochem. Soc.* **2007**, *154*, B427.

(60) Assuming a pO_2-independent $V_O^{\cdot\cdot}$ mobility, the experimental finding of an ionic conductivity of $\sigma_{ion} \propto (pO_2)^{-0.34}$ for $La_{0.74}Sr_{0.18}MnO_{3-\delta}$[10] implies $[V_O^{\cdot\cdot}] \propto (pO_2)^{-0.34}$.

(61) E_a of M2 is expected to be underestimated because the too exothermic overall DFT reaction enthalpy will also lower the reaction barriers. In mechanisms with $V_O^{\cdot\cdot}$ in the rate-determining step, this is more or less compensated by the too strong temperature dependence of $[V_O^{\cdot\cdot}]$ which also originates in the too negative DFT oxidation enthalpy.

JP909401G